Ionospheric density depletions around crustal fields at Mars and their connection to ion frictional heating

Hadi Madanian[1], Troy Hesse[1], Firdevs Duru[2], Marcin Pilinski[1], Rudy Frahm[3]

[1]Laboratory for Atmospheric and Space physics, University of Colorado Boulder, Boulder, CO 80303, USA
[2]Coe College, Cedar Rapids, IA 52402, USA
[3]Space Physics and Engineering Division, Southwest Research Institute, San Antonio, TX 78238, USA

Correspondence to: Hadi Madanian (hmadanian@gmail.com)

Abstract. Mars' ionosphere is formed through ionization of the neutral atmosphere by solar irradiance, charge exchange, and electron impact. Observations by Mars Atmosphere and Volatile EvolutioN (MAVEN) spacecraft have shown a highly dynamic ionospheric layer at Mars impacted by loss processes including ion escape, transport, and electron recombination. The crustal fields at Mars can also significantly modulate the ionosphere. We use MAVEN data to perform a statistical analysis of density depletions of ionospheric species (O^+, O_2^+, and electrons) around crustal fields. Events mostly occur when the crustal magnetic fields are radial, outward, and with a mild preference towards east in the planetocentric coordinates. We show that events near crustal fields are typically accompanied by an increase in suprathermal electrons within the depletion, either throughout the event or as a short-lived electron beam. However, no correlation between the changes in the bulk electron densities and suprathermal electron density variations is observed. Our analysis indicates that the temperature of the major ionospheric species, O_2^+, increases during most of the density depletion events, which could indicate that some ionospheric density depletions around crustal fields are a result of ion frictional heating.

1 Introduction

The solar extreme ultraviolet (EUV) and X-ray radiations at Mars can ionize neutral species (CO_2, O, N_2) to create ionospheric ions and suprathermal photoelectrons (Schunk and Nagy, 2009). Suprathermal photoelectrons and precipitating solar wind electrons can initiate further ionization through impacts with neutrals and cascade in energy to eventually form the bulk electron gas in the ionosphere. Through a series of chemical reactions, O_2^+ and O^+ become the most dominant ion species at Mars' ionosphere at altitudes above ~200 km, with O^+ having a longer scale height and requiring a smaller escape energy (Benna et al., 2015; Fowler et al., 2022; Haider et al., 2011; Withers et al., 2019). The peak of the dayside ionospheric layer at Mars is typically formed at around 110-150 km altitudes (Girazian et al., 2020; Vogt et al., 2017). Lack of a global dipole field at Mars and the short distance of the bow shock boundary from the surface makes the ionosphere highly susceptible to upstream effects. The ionosphere is highly variable due to variations in upstream solar wind conditions and changes in the amount of solar flux which varies by the solar zenith angle, seasons, and planetary orbit.

The Martian ionosphere can also be modulated by Mars' residual crustal magnetic fields that are mostly present in the southern hemisphere (Dubinin et al., 2016; González-Galindo et al., 2021; Withers et al., 2016). For instance, tailward transport rate is reduced near the crustal fields and O^+ ions seem to linger where they are generated on the dayside (Lundin et al., 2011). Strong crustal fields can also trap low energy ions and reduce the ion pickup and escape rate around these fields (Fan et al., 2019). Effects of crustal fields on electrons are more variable and less determined. Statistical studies have shown that electrons trapped on closed crustal field lines in general have longer lifetime and exhibit higher densities and lower temperatures compared to other places and these effects increase with altitude and are modestly affected by the solar wind conditions (Andrews et al., 2023; Flynn et al., 2017). In general, elevated plasma densities are observed near crustal fields (Andrews et al., 2015). On the nightside, suprathermal electrons that can ionize the ionosphere have limited access to the atmosphere around closed crustal magnetic fields resulting in smaller ion densities near crustal fields (Girazian et al., 2017). The ionopause, which appears as a steep gradient in the bulk electron density altitude profile data, is also suppressed around strong crustal fields as these fields limit the access of precipitating electrons (Chu et al., 2019).

Sudden ionospheric density depletions at Mars have been the topic of several previous studies. A density depletion is a sudden decrease (dip or hole) in the plasma density altitude profile inconsistent with the (on average) exponentially decreasing altitudinal change. Several statistical studies have indicated that although these depletions are observed across the entire Martian ionosphere, there is a tendency for observing these dropouts near the crustal fields (Basuvaraj et al., 2022; Duru et al., 2011; Withers, 2005). Early investigations on the topic using Mars Global Surveyor Radio Science experiment discussed depletions or "bite-outs" in anomalous ionospheric density profiles mainly observed near crustal magnetic fields at Mars (Withers, 2005). It was suggested that more analysis of these events is necessary to determine the nature of these events. Analysis of data from Neutral Gas and Ion Mass Spectrometer (NGIMS) (Mahaffy et al., 2015b) on the MAVEN spacecraft around these structures has shown that these electron deficit structures are bubble-like in shape and seem to be more frequent on the nightside (Basuvaraj et al., 2022). Duru et al. (2011) used data from Mars Advanced Radar for Subsurface and Ionospheric Sounding (MARSIS) instrument onboard the Mars Express spacecraft to analyze these structures on the nightside and near the terminator regions to show that some events are aligned with the onset of a photoelectron boundary. In a study of these depletions on the nightside of Mars using the same dataset, Cao et al. (2022) argued that while small amplitude depletions of bulk electrons could occur anywhere across the ionosphere, large amplitude depressions of the total electron content near strong crustal fields could be, although not always, related to shielding of precipitating suprathermal electrons. The co-occurrence (or lack thereof) of bulk electron depletion with suprathermal electrons has not been established so far.

A similar nomenclature was used for certain density structures at Venus' nightside ionosphere referred to as ionospheric density holes with generation mechanism associated with the radial extension of draped magnetic field lines around the planet where the plasma can flow and be depleted tailward (Brace et al., 1982). Certain density ridges and troughs in the Martian ionosphere could be compared to sporadic E-like layers at Earth' ionosphere near the equator where two counter-streaming plasma flows interact causing relative ion drifts (Collinson et al., 2020). However, the region of crustal magnetic

65 fields at Mars in some respect most likely resembles the polar cap regions of Earth where the geomagnetic fields have radial geometry at low altitudes and become more horizontal farther out. Density depletions in Earth's high-latitude ionospheric F-layer are commonly observed in incoherent scatter radar data (Bjoland et al., 2021). Such ionospheric troughs could be caused by enhanced electron dissociative recombination rates driven by warmer ions. Enhancement of the ion temperature increases the charge exchange rate with neutrals, e.g., O_2 and N_2, creating ion products that recombine quickly with electrons

70 leading to consumption of cold electrons and ions (Rodger et al., 1992).

In this paper, we focus our efforts on characterizing density depletions around crustal magnetic fields at Mars and perform a statistical analysis of plasma properties during these events. Irregular and unexpected depletions of the ionosphere can have major consequences for ion escape and space weather at Mars (González-Galindo et al., 2021; Xu et al., 2020; Cao et al., 2022). As such, it is important to investigate and characterize these events. The manuscript is organized as follows: in

75 Section 2 we introduce the data sources and our analysis methods and approach for event selection. Section 3 contains our observation results. We discuss the results in Section 4 and conclusions are provided in Section 5.

2 Methodology, Event Selection, and Data Sources

In this study, we use data from the MAVEN spacecraft. We survey Langmuir Probe and Wave (LPW) (Andersson et al., 2015) measurements between 2015 and 2022 for ionospheric density depletions. Due to the highly dynamic and turbulent

80 Martian ionosphere, our automated detection algorithm produced many false flags. As such, we identify these events through visual inspection. For each orbit leg, we inspect the electron density profile to identify an isolated depletion event showing the highest deviation from the general pattern of an exponentially decreasing profile (see the example in Figure 1). We skipped orbits with no or limited data points where the structure of the ionosphere cannot be observed, orbits with periapsis at high altitudes (above 400 km), and orbits that showed high amplitude variations and multiple depletions and

85 enhancements in the density profile. To quantify the closeness of a depletion event to the Martian crustal fields we define a proximity parameter ζ as:

$$\zeta = \sum_{i=x,y,z} \frac{\Sigma|B_{i,sc} - B_{i,m}|}{\Sigma|B_{i,m}|} \qquad (1)$$

where $B_{i,sc}$ is the spacecraft measurements of the magnetic field and $B_{i,m}$ is the crustal magnetic field modeled at the

90 position of the spacecraft (Morschhauser et al., 2014). $B_{i,m}$ and $B_{i,sc}$ must be in the same coordinate system. ζ provides an estimate of the crustal field prevalence or a measure of closeness of the observations to the crustal fields at Mars. Lower ζ values indicate more contributions from the crustal field with $\zeta = 0$ meaning observed fields are identical to model predictions. Contributions of external magnetic fields from the solar wind or perturbation to the field generated locally by instabilities or currents lead to increased deviation of observations from the model and higher values of ζ. In deriving

95 Equation 1, effects of generic similarities between time series (constant arrays), singularities, and absolute strength of the fields are also considered.

Figure 1 shows an example of an ionospheric depletion event on 2 November 2016. Panel a shows three components of the observed magnetic field (markers) and the modeled crustal fields (solid lines). The area between the curves along each component (numerator in Equation 1) is used in determining ζ. This event has $\zeta = 1.16$. The proximity parameter for all

100 events varies between 0.19 to 4.92, with a mean value of 2.18 and a median of 1.91. Panel b in Figure 1 shows the electron density measurements by LPW with a depletion between 04:08:00 and 04:09:38 UTC. The density of suprathermal electrons measured by SWEA increases during this time as seen in Panel c. Panel d indicates that densities of ionospheric heavy ions O^+ and O_2^+, as measured by STATIC also decrease during this event.
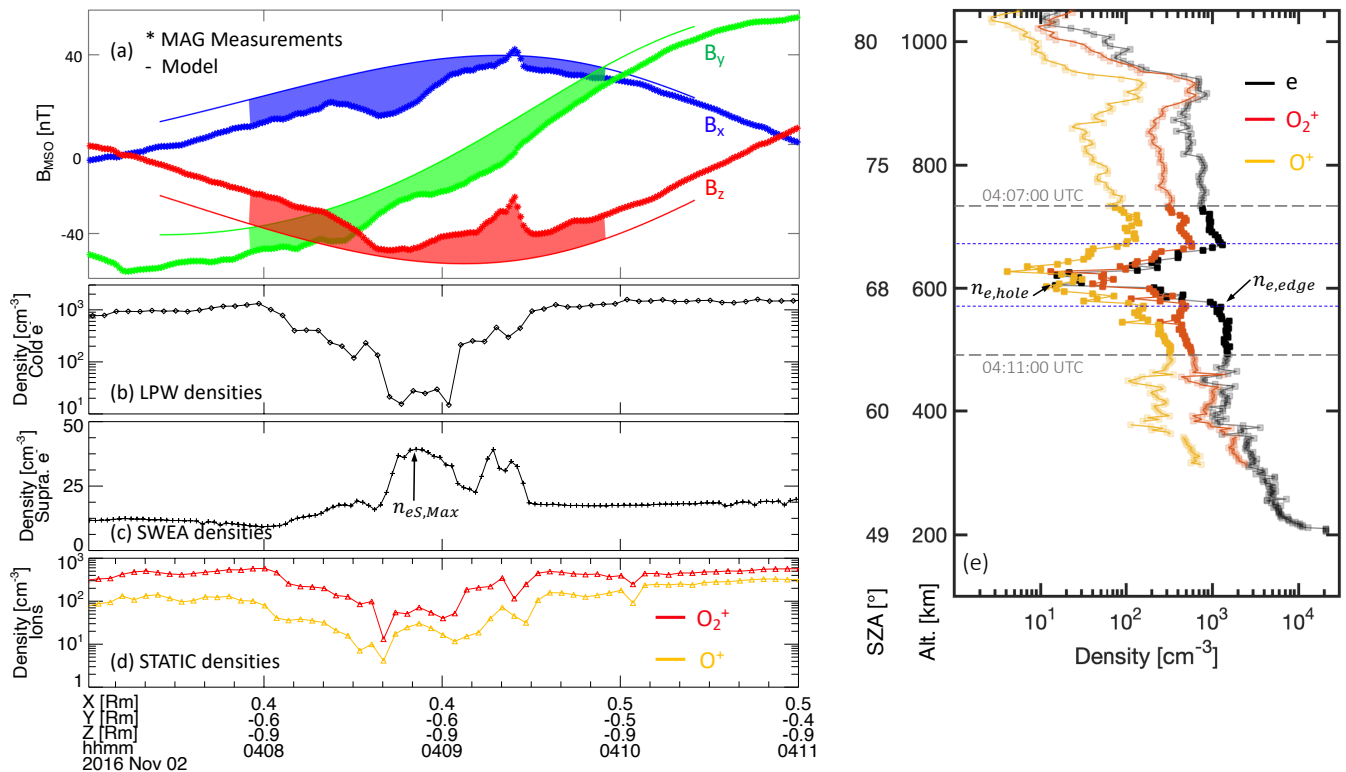
Figure 1. (a) Magnetic field measured by the MAVEN magnetometer (asterisks) and the modeled crustal fields (solid lines) in the Mars Solar Orbital (MSO) coordinates, (b) bulk electron density measurement by LPW, (c) suprathermal electron density measurements by SWEA, $n_{eS,Max}$ is the maximum suprathermal electron density inside the depletion, (d) STATIC density measurements of O^+ (yellow) and O_2^+ (red) ions, (e) Altitude and solar zenith angle (SZA) density profiles. The horizontal dashed grey lines show the extent of data shown in time series panels on the left, while the depletion event boundaries are marked with dashed blue lines. $n_{e,hole}$ and $n_{e,edge}$ are the bulk electron density inside and outside the

depletion event.

We focus on density depletion events with $\zeta < 5$. This threshold is set by visual inspection of several events as we determined that for events with $\zeta < 5$, spacecraft measurements certainly contain contributions from crustal fields. 242 events met this criterion. STATIC ion density data are available for 135 of these events. O_2^+ ion temperatures can be derived from STATIC measurements and are available during 83 events. Limitations dictated by spacecraft attitude, instrument pointing and ram direction, and ion abundance at a given altitude restrict the available times when STATIC measurements can be properly calibrated for derivation of O_2^+ ion temperatures. For details of the STATIC calibration process and derivation of ion densities and temperatures readers are referred to the STATIC instrument paper and follow up calibration studies (McFadden et al., 2015; Hanley et al., 2021; Fowler et al., 2022). SWEA measurements of suprathermal electrons over the full energy range (3 eV to 4.6 keV) are available during 95 events. This is mainly due to a change made in SWEA's energy sweep table during 2020 which raised the minimum scan energy which limits the number of events with accurate measurements of all suprathermal ions. Nevertheless, available data provide a reasonable sample size to analyze the behavior of suprathermal electrons.
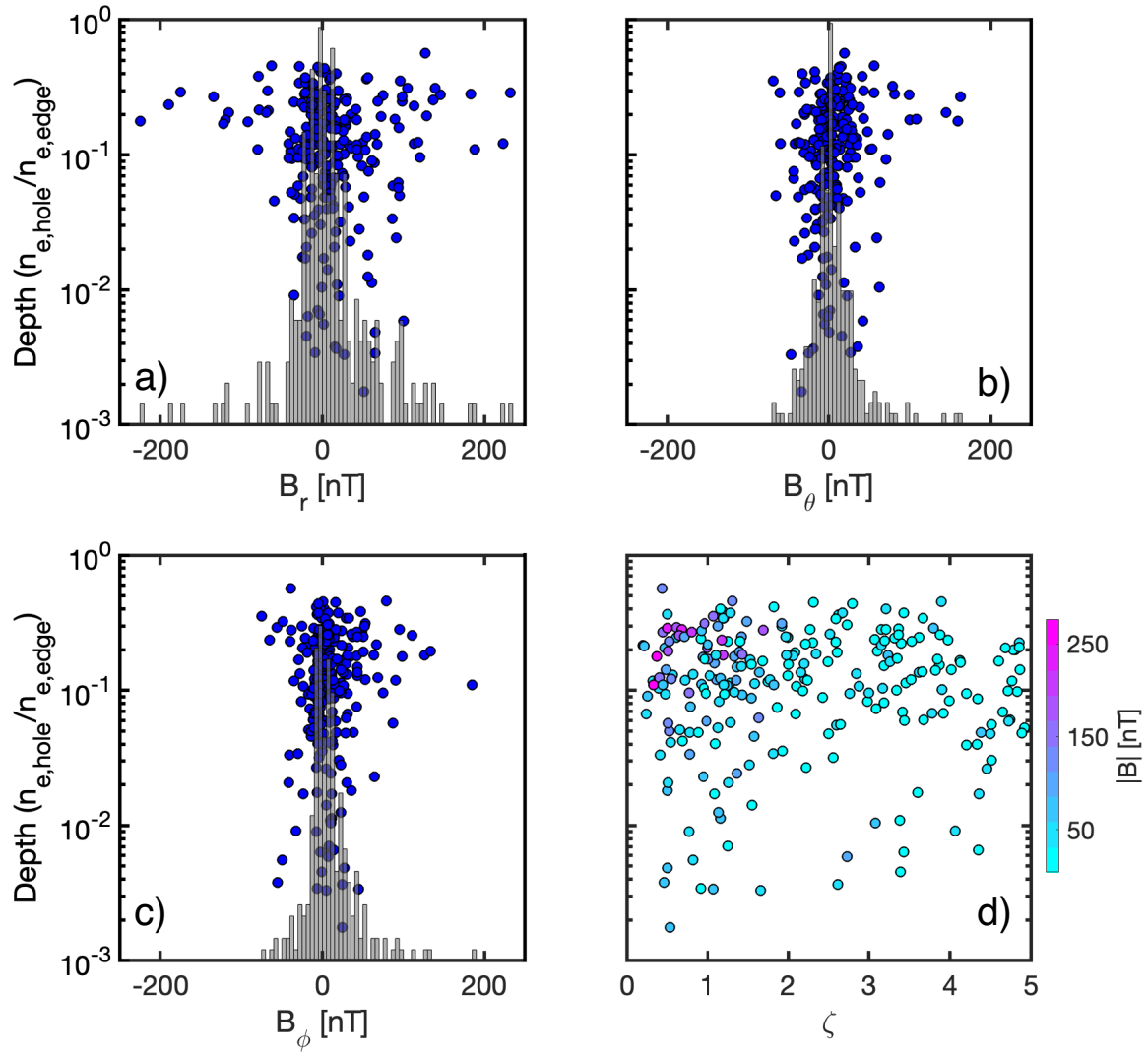
Figure 2. Distribution of depletion depth versus (a) B_r, (b) B_θ, (c) B_φ, and (d) ζ. Normalized bar plots in grey in the background on Panels a - c show the relative occurrence rate of events. Data points on Panel d are color coded by the modeled crustal magnetic field strength.
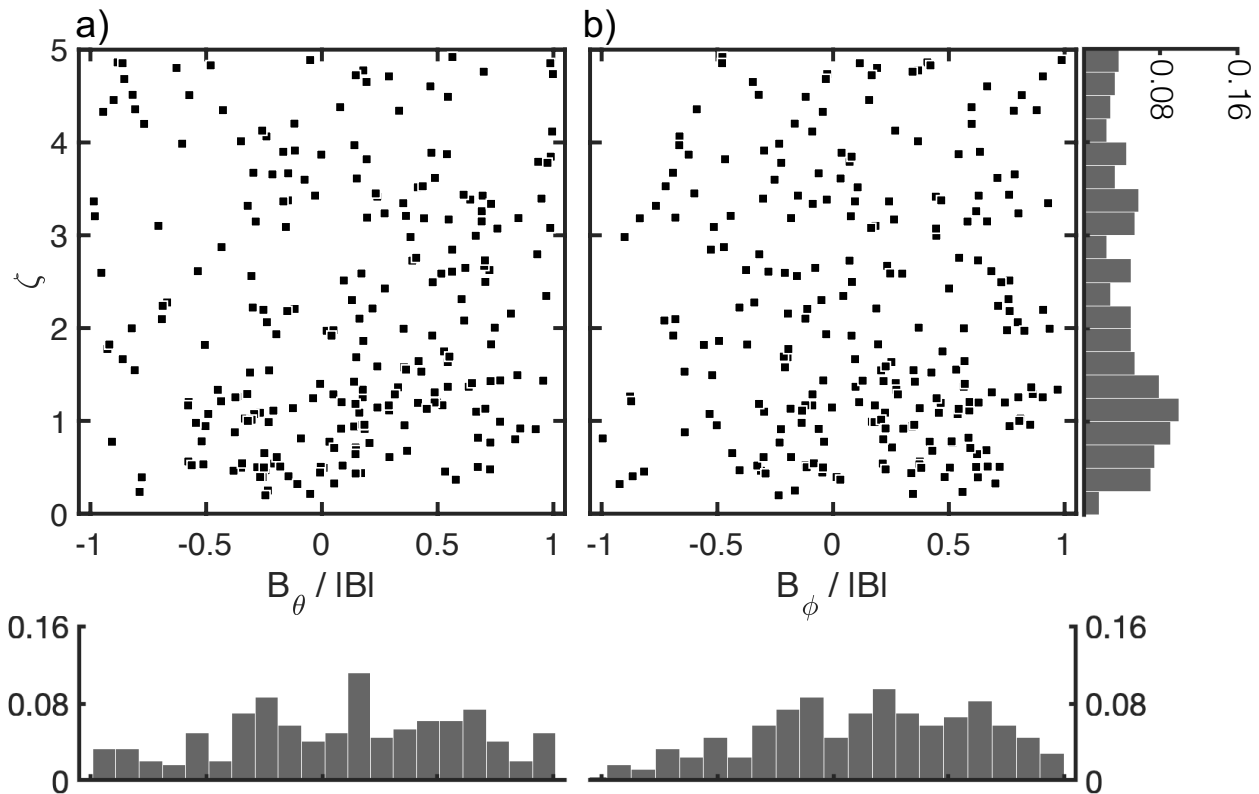
Figure 3. Event distributions as a function of the modeled crustal magnetic field direction along (a) θ and (b) φ. The normalized probability distribution histogram for each component is shown below the panel, with the distribution for ζ shown to the right.

3 Observations

The depth of a density depletion is defined as the ratio of the lowest bulk electron density inside the hole ($n_{e,hole}$) to the highest electron density of either sides/edges of the depletion ($n_{e,edge}$). The event distributions along three components of the magnetic field taken at the lowest density point of the depletion are shown in Figure 2. The magnetic field vectors are in spherical coordinates of the Mars body-fixed planetocentric frame. In this coordinate system, r is along planet's radius, and φ and θ are polar coordinates (parallel to the surface) changing between [0°, 360°] and [-90°, 90°], respectively. Comparing Figure 2a to 2b and 2c, we find that the radial component of the magnetic field shows the highest level of variations compared to field components parallel to the surface, with perhaps a slight preference towards $+B_r$, or when the crustal fields exit the surface. The histogram of the probability distribution for each field component is overplotted on each panel.

Panel d shows the depletion depths as a function of ζ, and no apparent correlation is seen between these two parameters. Data points on this panel are color coded by the magnetic field strength. Several events with relatively high magnetic field

strength (purple data points) appear at $\zeta < 2$ (i.e., fields are mostly dominated by strong crustal fields). Though, as Equation 1 indicates, ζ is normalized by the strength of the field components and is only a measure of the proximity of the event and spacecraft to any crustal field regardless of the field strength.

135   In Panels a and b of Figure 3, we show the distribution of ζ as a function of normalized field components $\widehat{B}_\theta$ and $\widehat{B}_\varphi$, respectively. Corresponding normalized probability distribution histograms are shown below each panel, while the histogram to the right shows the distribution in ζ with a peak at $\zeta \sim 1$. The distribution in Panel a exhibits a peak at $\widehat{B}_\theta = 0.2$, though it is not immediately clear if there is any preference on $\widehat{B}_\theta$. Events appear to be more frequent along $+\widehat{B}_\varphi$, suggesting that the depletions are found more likely around crustal magnetic fields pointing eastward. The significance of such dependence and

140   possible relationship to the planetary rotation will be investigated in future studies.
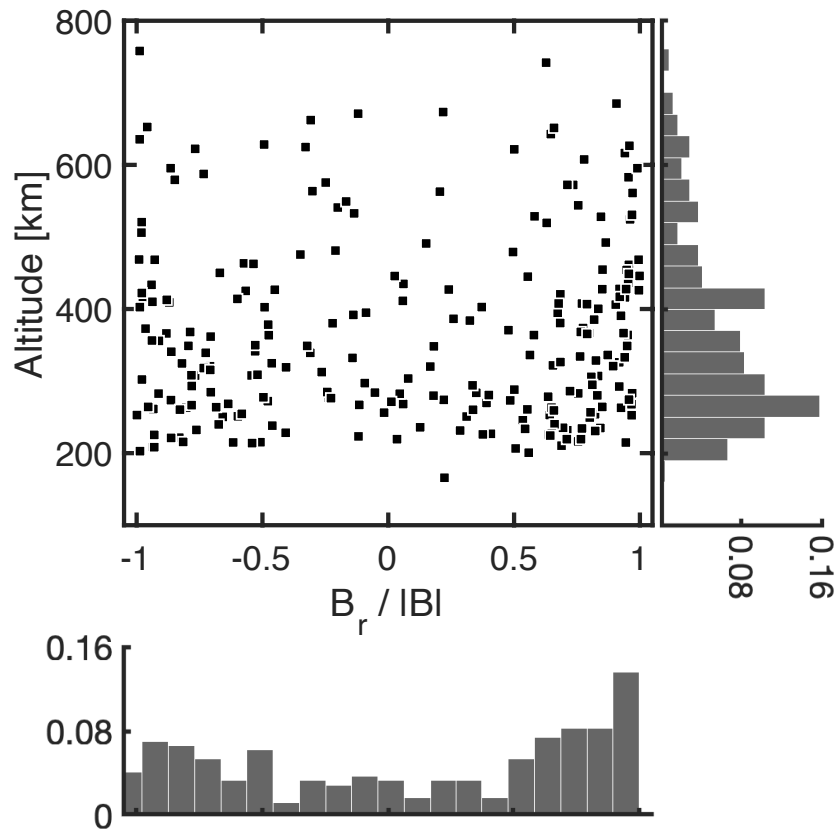
Figure 4. Distribution of events in altitude and along the normalized radial component of the crustal magnetic fields. Histograms below the figure and to the right show the normalized probability distribution of events in $\widehat{B}_r$ and altitude.

As we discussed in Panel a of Figure 2, there is a preference for observing density depletions when the crustal fields have a radial orientation (i.e., exiting the Martian surface). This preference is clearly seen in Figure 4, where the probability distribution of events along $\widehat{B}_r$ is shown. The distribution of events in altitude exhibits two major peaks, one observed at ~ 265 km and the other at ~ 410 km. The magnetic field data in Figures 2, 3, and 4 are from the crustal field model. We also performed a similar analysis using spacecraft measurements of the magnetic field in the middle of each depletion. The events appear more evenly distributed along $\widehat{B}_r$, $\widehat{B}_\theta$ and $\widehat{B}_\varphi$ when in-situ spacecraft data are used. In-situ magnetic field measurements include effects of upstream magnetic field as well as fields due to local currents which can change the modeled field orientation.

Previous studies have shown that the flux of suprathermal electrons can increase within some depletion events and decrease or even disappear for other events (Cao et al., 2022; Duru et al., 2023, 2011; Nielsen et al., 2007). The cause and the underlying process that controls the suprathermal electrons within the ionospheric density depletion is not well understood. Here, by using MAVEN observations of different electron populations (i.e., bulk/thermal and suprathermal) we choose a more quantitative approach to study the dynamics of suprathermal electrons within depletion events near crustal fields. It appears that events can be divided into two main categories. Increase of suprathermal electron fluxes within depletion events can be through an increase in the flux of suprathermal electrons over almost the entire event, or via a short beam-like surge of electrons in the middle of the depletion or near the boundaries. We define three measures to quantify electron density variations. $\Delta n_{e,C} = n_{e,edge} - n_{e,hole}$ is the change in cold or bulk electron density between the lowest density within the depletion and the measured density outside the depletion. $\Delta n_{e,S} = n_{eS,Max} - n_{eS,edge}$ is the difference between the maximum suprathermal electron density inside the depletion ($n_{eS,Max}$) and the density outside the depletion ($n_{eS,edge}$) and gives an estimate of the increase or decrease in suprathermal electrons, either throughout the depletion or as a sudden pulse. We also define $\delta n_{e,S} = n_{eS,Max} - \tilde{n}_{eS}$ which is the difference between $n_{eS,Max}$ and the average suprathermal electron density over the depletion period ($\tilde{n}_{eS}$). A higher value of $\delta n_{e,S}$ is indicative of a stronger and more intense suprathermal electron beam. The outside (ambient plasma) density measures are the maximum of the density measurements at both edges of the depletion (see Panel e in Figure 1).
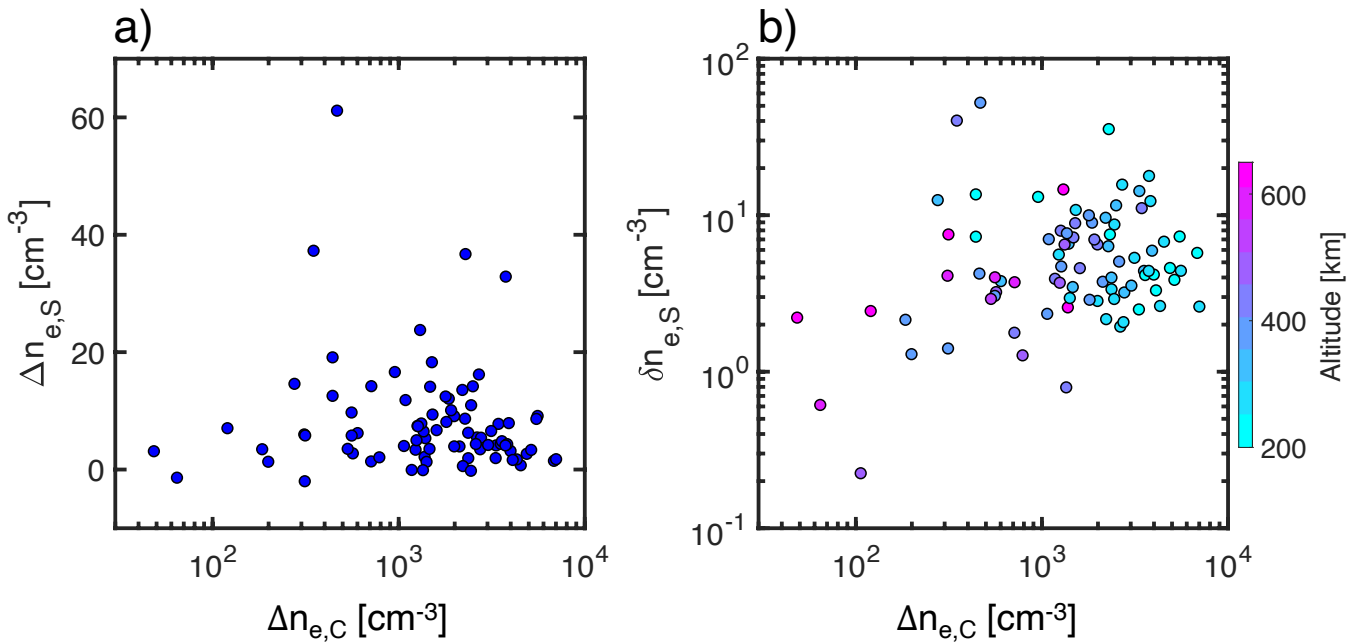
Figure 5. Suprathermal electron density variations as a function of change in the bulk electron density across the depletions. Panel a shows the maximum difference in suprathermal electron density between inside and outside the depletion. Panel b shows the difference between the maximum suprathermal electron density and the average suprathermal density inside the depletions. Data points in Panel b are color coded by altitude.

170

Panel a in Figure 5 shows the dependence of $\Delta n_{e,S}$ on $\Delta n_{e,C}$. All depletion events but six are accompanied by an enhancement in the flux of suprathermal electrons. This is perhaps a distinguishing aspect between events near the crustal fields considered in this study and those discussed in previous studies of depletions across the entire ionosphere for which no

175 clear pattern in the abundance of suprathermal electrons are found. Density variations of the suprathermal and bulk electron populations during depletion events do not seem to be correlated which is inconsistent with an acceleration mechanism that shifts part of the bulk electron population to higher energies while creating the density bite-out. In Panel b of Figure 5, variations of δn_{eS} versus $\Delta n_{e,C}$ are shown. Data points are colored by the altitude at which the depletions are observed. Events at low altitudes (cyan colors), where ionospheric densities are typically higher and crustal fields stronger, exhibit high

180 values of $\Delta n_{e,C}$ (> 10^3 cm^{-3}) compared to events at other altitudes. $\delta n_{e,S}$ for these events also increases by at least a factor of 2, suggesting that beams of suprathermal electrons could occur at lower altitudes where crustal fields are stronger.
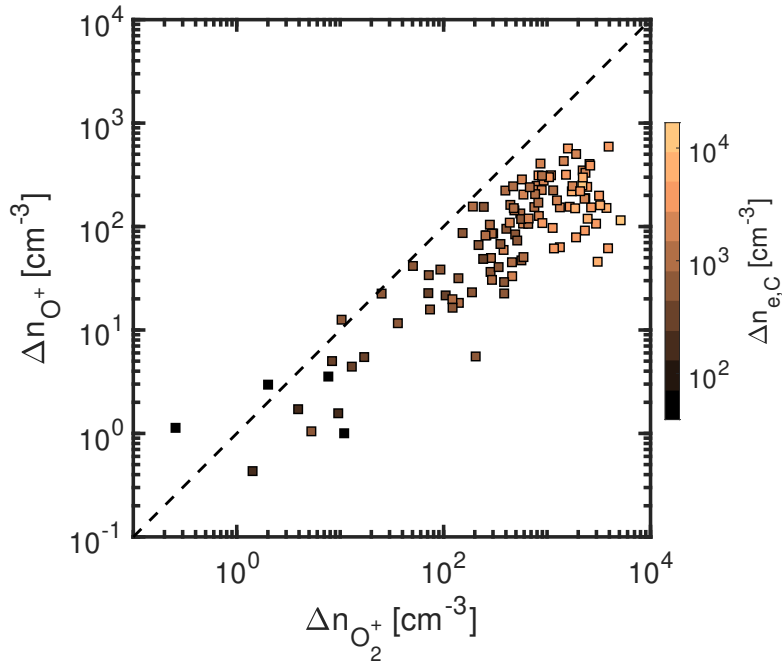
Figure 6. Density variations of most abundant ionospheric species, O^+ and O_2^+. Points are color coded by corresponding changes in the bulk electron density $\Delta n_{e,C}$. Eight depletion events which exhibit increased ion densities within the depletion from to the ambient plasma are not shown.

As we discussed in Figure 1 Panel d, ionospheric ions follow a similar depletion pattern to that of bulk electrons during these events. In Figure 6, we analyze the density variations of the most abundant ionospheric ion species, O^+ and O_2^+. There are higher density variations in O_2^+ at lower altitudes with increasing $\Delta n_{e,C}$ (shown with the color scale). O_2^+ is the dominant ion species at low altitudes and has a shorter scale height compared to O^+. Results shown in this figure are consistent with previous studies that analyzed ion densities using NGIMS measurements (Basuvaraj et al., 2022). The strong correlation observed between the depletion of cold electrons and ions in the ionosphere indicates that a similar physical mechanism is in play removing electrons and all ions from the ionosphere. The likely candidate mechanism would be ion-electron recombination which consumes both electrons and ions.
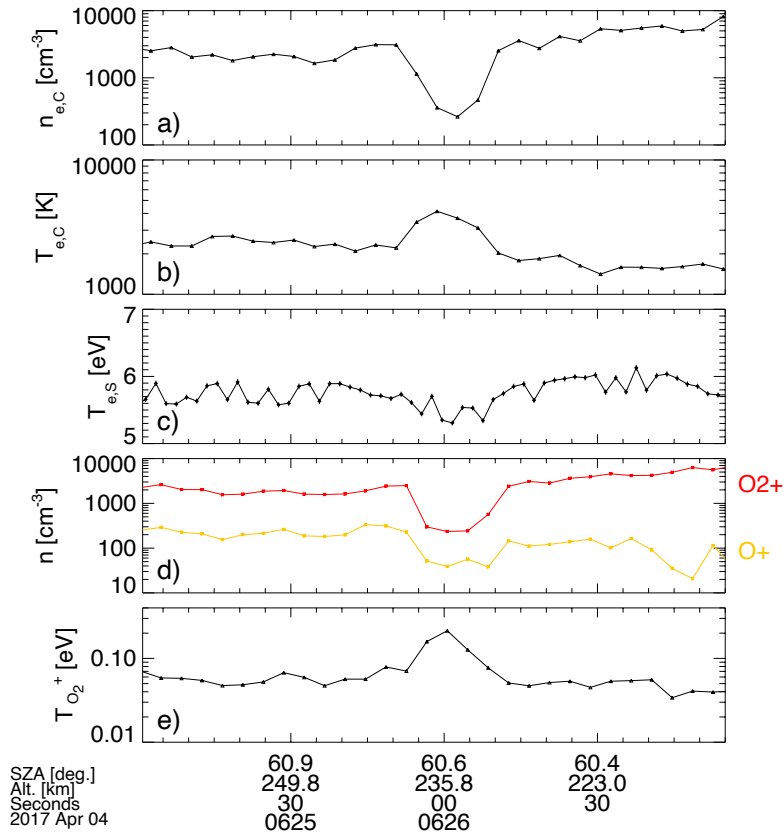
Figure 7. Overview of a density depletion event on 4 April 2017 at 06:26:00 UTC. Panels show (a) the density and (b) temperature of bulk electrons, (c) the suprathermal electron temperatures, (d) O^+ (yellow) and O_2^+ (red) densities, and (e) O_2^+ temperatures.

Figure 7 shows another example of a density hole in the Martian ionosphere. LPW bulk electron and STATIC ion density

195 measurements are shown in Panels a and d, respectively. We also show the temperatures of bulk electrons, suprathermal electrons, and ions in Panels b, c, and e as measured by LPW, SWEA and STATIC instruments, respectively. The temperature of bulk electrons and ions increases during the depletion while the suprathermal electron temperature decreases. Regarding the bulk electron temperature, we should note that the electron plasma parameters in a Langmuir probe are obtained from the probe characteristic current-voltage (I-V) curve. The slope of this curve, which is inversely proportional to

200 the electron temperature, can decrease due to the reduced electron saturation current. However, that current can decrease if a plasma sink is actively present in the plasma (as is the case for density holes,) rather than reflecting an actual change in the temperature of the electron gas. It is therefore likely that the increase in the bulk electron temperature is an artifact of sudden depletion of the cold electron gas within the density hole which leaves only "warm" electrons to be probed by the LPW, rather than heating of electrons by a physical process and increase in their thermal velocity. On the other hand, the

205 temperatures derived from electrostatic analyzers (SWEA, STATIC) data are determined from the energy extent (width) of the particles entering the instrument and thus directly relate to the average temperature of charged particles.

O_2^+ ions within the density depletion as shown in Panel e of Figure 7 have higher temperatures than the surrounding plasma. The higher ion temperature could be a sign of ion frictional heating which arises due to a relative ion drift in the frame of
210 neutral species. External electric fields such as the convection electric field, or atmospheric waves and other dynamic processes can cause a velocity difference between ions and neutrals. The electric field creates $\mathbf{E} \times \mathbf{B}$ drift in the plasma which increases the ion drift. Motion of the background neutral atmosphere relative to ions also leads to a velocity drift. In either case, at large enough drift speeds, frictional heating occurs which increases the ion temperatures.

As shown in Figure 8, ion temperatures inside most depletion events show an increase. In some event the ion temperatures at
215 the center of the depletion where the ion densities are at a minimum, are not well determined. Depletion and reduced counts of ions within these events undermines the reliable determination of ion temperatures. Figure 8 also indicates that events clustered at around 400 km altitude show more drastic variations in ion temperatures, which could be associated with increased heating of ions due to their drift relative to neutrals. Such a velocity difference typically increases with altitude, while the heating process itself is bound by the abundance of the local neutral species.

220
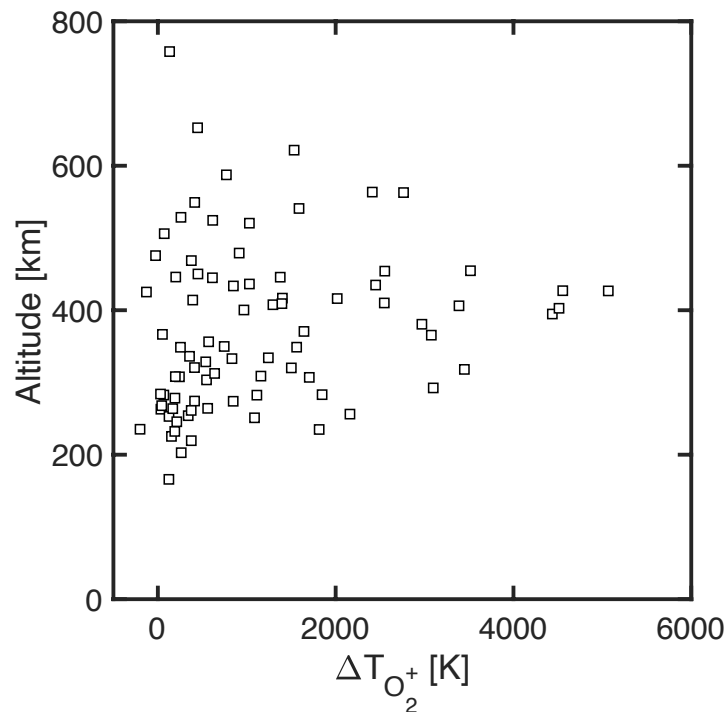
Figure 8. Change in the temperature of O_2^+ ions inside the depletions from the ambient plasma, in Kelvin, as a function of altitude.

4 Discussion

Physical processes that cause the ionospheric density depletions at Mars are not well understood. By studying these events near crustal magnetic fields, we focus on generation mechanisms that can be mapped along crustal magnetic field lines, and that can impact charged particles at higher altitudes. Ion pickup is a major loss process at high altitudes of Mars (Cravens et al., 2002). In Figures 1 and 6, we show that ions with different masses are depleted at about the same rate, indicating that ion pickup cannot explain the loss process, as it operates slower on heavier ions (O_2^+ in this case). Furthermore, electrodynamical forces in the ionosphere tend to have opposite impacts on ions versus electrons.

In the Martian upper atmosphere, CO_2 remains the most abundant neutral species up to ~200 km altitude, above which atomic oxygen becomes the dominant neutral constituent with lower abundances of N_2 and O_2 (Benna et al., 2015; Mahaffy et al., 2015a). At altitudes above 200 km, O_2^+ and O^+ are the most abundant ionospheric species. Chemical loss of O^+ ions is a slow process. This is mainly due to the small electron recombination and ion-neutral reaction rate coefficients. Relevant reactions and associated rates are listed below (Schunk and Nagy, 2009):

$$O^+ + N_2 \rightarrow NO^+ + N \qquad 1.2 \times 10^{-12} \text{ cm}^3\text{s}^{-1} \qquad (2)$$

$$O^+ + O_2 \rightarrow O_2^+ + O \qquad 2.0 \times 10^{-11} \text{ cm}^3\text{s}^{-1} \qquad (3)$$

$$O^+ + CO_2 \rightarrow O_2^+ + CO \qquad 1.1 \times 10^{-9} \text{ cm}^3\text{s}^{-1} \qquad (4)$$

$$O_2^+ + NO \rightarrow NO^+ + O_2 \qquad 4.6 \times 10^{-10} \text{ cm}^3\text{s}^{-1} \qquad (5)$$

$$O^+ + e \rightarrow O \qquad 1.76 \times 10^{-10} T_e^{-0.7} \qquad (6)$$

$$O_2^+ + e \rightarrow O + O \qquad 1.3 \times 10^{-5} T_e^{-0.7} \qquad (7)$$

$$NO^+ + e \rightarrow N + O \qquad 6.93 \times 10^{-6} T_e^{-0.5} \qquad (8)$$
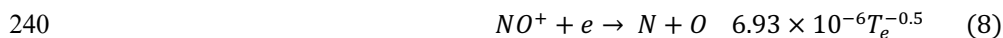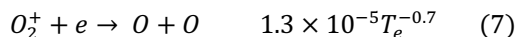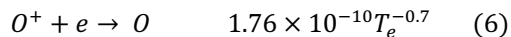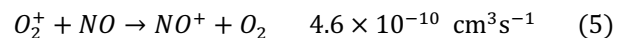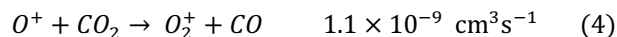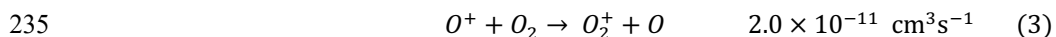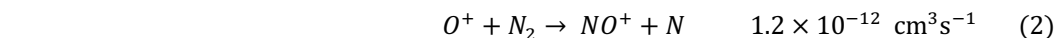
While the reaction of O^+ ions with neutral species is slow, the byproducts of reactions in Equations 2 – 4, namely O_2^+ and NO^+ ions, can quickly recombine with bulk electrons, removing both ions and electrons from the plasma in the process. Recombination of O_2^+ ions with electrons is orders of magnitude faster compared to O^+. In addition, the ion-neutral reaction rate coefficients are energy dependent and increase with ion temperature (Rodger et al., 1992; St.-Maurice and Torr, 1978; Viggiano et al., 1992). For instance, the reaction in Equation 3 can be an order of magnitude faster for a temperature increase of ~8,000 K (or 0.68 eV) (Rodger et al., 1992, Figure 8). Frictional heating increases the ion temperature which results in increased ion-neutral reaction rates and production of ions that recombine faster with electrons and create localized density depletion zones near crustal fields.

Data in Figures 7 and 8 indicate that ion temperatures clearly increase within the depletion events. The exact process (external electric fields or atmospheric disturbances) that initiates the frictional heating in the ionosphere is left for a future study. But since at low altitudes the O^+ gyrofrequency is smaller than the ion-neutral collision frequency, ions are likely to undergo at least one collision before they can complete a full gyration around the magnetic field and can be considered

nonmagnetized, while electrons are magnetized. Electron-ion recombination removes both electrons and ions creating a density depletion in the plasma. In return, we would expect to see an increase in the neutral density. However, since the change in the plasma density is on the order of a few thousands cm^{-3} or less, it is difficult to detect such small variations in a background neutral atmosphere of $10^5 - 10^8$ cm^{-3}.

For radial crustal fields, the $\mathbf{E} \times \mathbf{B}$ can only result in horizontal drift and heating of ions parallel to the Martian surface. This could have an effect on these depletions to appear as elongated horizontal structures in spacecraft observations (Basuvaraj et al., 2022). When exposed to the solar extreme ultraviolet flux, the new neutral products from the dissociative recombination will be photoionized creating new pairs of photoelectrons and ions, which could explain the surge of suprathermal electrons within these structures (Duru et al., 2011).

5 Conclusion

In this statistical study, we focus on ionospheric density depletion events observed in the vicinity of crustal fields at Mars. We define the proximity parameter ζ to quantify the proximity of observed events to Martian crustal magnetic fields and select a subset of events. We use MAVEN observations between 2015 and 2022. Ion measurements from STATIC, cold electron measurements from LPW, magnetic field data from MAG, and suprathermal electron measurements from the SWEA instrument around these events are analyzed. Our survey of MAVEN-LPW ionospheric density profiles results in 1570 density depletion events. We then check the crustal field proximity condition on these events and obtain 242 events with the proximity parameter $\zeta < 5$. Events below this threshold seem to show a recognizable signature of crustal fields. To avoid and minimize density variations due to the solar zenith angle, seasons, and heliocentric distance on our analysis, instead of absolute density values, we compare the differences of the ionospheric densities between inside and outside the depletion events to quantify these structures (Andrews et al., 2023). We however note that a limitation of single point measurements is that depending on the spacecraft trajectory and path through a three-dimensional density structure, the observed density variations may not reflect the actual structure depth.

We investigate variations of different plasma populations within the density depletions and find that suprathermal electrons are almost always present within the density depletions near crustal fields. We show that increase in the ion temperature during some events could be associated with ion frictional heating, which could also be causing the depletion through a two-step process. Heating of ions increases the charge exchange reaction rates. This is followed by electron dissociative recombination of ions which removes both electrons and ions creating isolated plasma depletions.

Data availability

All data presented in the figures are publicly available on the Planetary Data System https://pds.nasa.gov and mirrored at http://sprg.ssl.berkeley.edu/data/maven/data/sci/. LPW density and temperatures are available through

pds://PPI/maven.lpw.derived/data/lp-nt. STATIC density and temperature data can be accessed at http://sprg.ssl.berkeley.edu/data/maven/data/sci/sta/l3. The software used for data retrieval, analysis, and creating figures is
285 publicly available through https://spedas.org.

Author contribution

HM conceptualized the idea, defined the analyses, and carried them out. TH, FD, and RF performed parts of the data analysis and event selections. MP assisted with NGIMS data analysis. HM prepared the manuscript with contributions from all co-authors.

290 **Competing interests**

The authors declare that they have no conflict of interest.

Acknowledgments

We acknowledge the support from the MAVEN contract to the Laboratory for Atmospheric and Space Physics (LASP) at the University of Colorado in Boulder.

295 **References**

Andersson, L., Ergun, R. E., Delory, G. T., Eriksson, A., Westfall, J., Reed, H., McCauly, J., Summers, D., and Meyers, D.: The Langmuir Probe and Waves (LPW) Instrument for MAVEN, Space Sci Rev, 195, 173–198, https://doi.org/10.1007/s11214-015-0194-3, 2015.

Andrews, D. J., Edberg, N. J. T., Eriksson, A. I., Gurnett, D. A., Morgan, D., Němec, F., and Opgenoorth, H. J.: Control of
300 the topside Martian ionosphere by crustal magnetic fields, J. Geophys. Res. Space Physics, 120, 3042–3058, https://doi.org/10.1002/2014JA020703, 2015.

Andrews, D. J., Stergiopoulou, K., Andersson, L., Eriksson, A. I. E., Ergun, R. E., and Pilinski, M.: Electron Densities and Temperatures in the Martian Ionosphere: MAVEN LPW Observations of Control by Crustal Fields, JGR Space Physics, 128, e2022JA031027, https://doi.org/10.1029/2022JA031027, 2023.

305 Basuvaraj, P., Němec, F., Němeček, Z., and Šafránková, J.: Ionospheric Plasma Depletions at Mars Observed by the MAVEN Spacecraft, JGR Planets, 127, https://doi.org/10.1029/2022JE007302, 2022.

Benna, M., Mahaffy, P. R., Grebowsky, J. M., Fox, J. L., Yelle, R. V., and Jakosky, B. M.: First measurements of composition and dynamics of the Martian ionosphere by MAVEN's Neutral Gas and Ion Mass Spectrometer, Geophysical Research Letters, 42, 8958–8965, https://doi.org/10.1002/2015GL066146, 2015.

310 Bjoland, L. M., Ogawa, Y., Løvhaug, U. P., Lorentzen, D. A., Hatch, S. M., and Oksavik, K.: Electron Density Depletion Region Observed in the Polar Cap Ionosphere, JGR Space Physics, 126, e2020JA028432, https://doi.org/10.1029/2020JA028432, 2021.

Brace, L. H., Theis, R. F., Mayr, H. G., Curtis, S. A., and Luhmann, J. G.: Holes in the nightside ionosphere of Venus, J. Geophys. Res., 87, 199, https://doi.org/10.1029/JA087iA01p00199, 1982.

315 Cao, Y., Niu, D., Liang, W., Cui, J., Wu, X., Wan, X., Zhong, J., Li, L., Rong, Z., and Wei, Y.: Total electron content depression in the nightside Martian ionosphere: statistical results from Mars Express MARSIS measurements and implications, Monthly Notices of the Royal Astronomical Society, 519, 2262–2267, https://doi.org/10.1093/mnras/stac3641, 2022.

Chu, F., Girazian, Z., Gurnett, D. A., Morgan, D. D., Halekas, J., Kopf, A. J., Thiemann, E. M. B., and Duru, F.: The Effects 320 of Crustal Magnetic Fields and Solar EUV Flux on Ionopause Formation at Mars, Geophys. Res. Lett., 46, 10257–10266, https://doi.org/10.1029/2019GL083499, 2019.

Collinson, G. A., McFadden, J., Grebowsky, J., Mitchell, D., Lillis, R., Withers, P., Vogt, M. F., Benna, M., Espley, J., and Jakosky, B.: Constantly forming sporadic E-like layers and rifts in the Martian ionosphere and their implications for Earth, Nat Astron, 4, 486–491, https://doi.org/10.1038/s41550-019-0984-8, 2020.

325 Connerney, J. E. P., Espley, J., Lawton, P., Murphy, S., Odom, J., Oliversen, R., and Sheppard, D.: The MAVEN Magnetic Field Investigation, Space Sci Rev, 195, 257–291, https://doi.org/10.1007/s11214-015-0169-4, 2015.

Cravens, T. E., Hoppe, A., Ledvina, S. A., and McKenna-Lawlor, S.: Pickup ions near Mars associated with escaping oxygen atoms: PICKUP IONS NEAR MARS, J. Geophys. Res., 107, SMP 7-1-SMP 7-10, https://doi.org/10.1029/2001JA000125, 2002.

330 Dubinin, E., Fraenz, M., Andrews, D., and Morgan, D.: Martian ionosphere observed by Mars Express. 1. Influence of the crustal magnetic fields, Planetary and Space Science, 124, 62–75, https://doi.org/10.1016/j.pss.2016.02.004, 2016.

Duru, F., Gurnett, D. A., Morgan, D. D., Winningham, J. D., Frahm, R. A., and Nagy, A. F.: Nightside ionosphere of Mars studied with local electron densities: A general overview and electron density depressions: NIGHTSIDE IONOSPHERE OF MARS, J. Geophys. Res., 116, n/a-n/a, https://doi.org/10.1029/2011JA016835, 2011.

335 Duru, F., Frahm, R. A., Hughes, D., Caplice, T., Pierce, J., and Madanian, H.: Local Electron Density Depletions in the Martian Upper Ionosphere Obtained From MARSIS: Comparison With ASPERA-3, and MAVEN, and the Connection With Crustal Magnetic Fields, JGR Space Physics, 128, e2023JA031327, https://doi.org/10.1029/2023JA031327, 2023.

Fan, K., Fraenz, M., Wei, Y., Han, Q., Dubinin, E., Cui, J., Chai, L., Rong, Z., Zhong, J., Wan, W., Mcfadden, J., and Connerney, J. E. P.: Reduced Atmospheric Ion Escape Above Martian Crustal Magnetic Fields, Geophys. Res. Lett., 46, 340 11764–11772, https://doi.org/10.1029/2019GL084729, 2019.

Flynn, C. L., Vogt, M. F., Withers, P., Andersson, L., England, S., and Liu, G.: MAVEN Observations of the Effects of Crustal Magnetic Fields on Electron Density and Temperature in the Martian Dayside Ionosphere, Geophysical Research Letters, 44, https://doi.org/10.1002/2017GL075367, 2017.

Fowler, C. M., McFadden, J., Hanley, K. G., Mitchell, D. L., Curry, S., and Jakosky, B.: In-Situ Measurements of Ion 345 Density in the Martian Ionosphere: Underlying Structure and Variability Observed by the MAVEN-STATIC Instrument, JGR Space Physics, 127, https://doi.org/10.1029/2022JA030352, 2022.

Girazian, Z., Mahaffy, P., Lillis, R. J., Benna, M., Elrod, M., Fowler, C. M., and Mitchell, D. L.: Ion Densities in the Nightside Ionosphere of Mars: Effects of Electron Impact Ionization, Geophys. Res. Lett., 44, 11,248-11,256, https://doi.org/10.1002/2017GL075431, 2017.

350 Girazian, Z., Luppen, Z., Morgan, D. D., Chu, F., Montabone, L., Thiemann, E. M. B., Gurnett, D. A., Halekas, J., Kopf, A. J., and Němec, F.: Variations in the Ionospheric Peak Altitude at Mars in Response to Dust Storms: 13 Years of Observations From the Mars Express Radar Sounder, J. Geophys. Res. Planets, 125, https://doi.org/10.1029/2019JE006092, 2020.

González-Galindo, F., Eusebio, D., Němec, F., Peter, K., Kopf, A., Tellmann, S., and Paetzold, M.: Seasonal and
355 Geographical Variability of the Martian Ionosphere From Mars Express Observations, JGR Planets, 126, https://doi.org/10.1029/2020JE006661, 2021.

Haider, S. A., Mahajan, K. K., and Kallio, E.: Mars ionosphere: A review of experimental results and modeling studies, Rev. Geophys., 49, RG4001, https://doi.org/10.1029/2011RG000357, 2011.

Hanley, K. G., McFadden, J. P., Mitchell, D. L., Fowler, C. M., Stone, S. W., Yelle, R. V., Mayyasi, M., Ergun, R. E.,
360 Andersson, L., Benna, M., Elrod, M. K., and Jakosky, B. M.: In Situ Measurements of Thermal Ion Temperature in the Martian Ionosphere, JGR Space Physics, 126, https://doi.org/10.1029/2021JA029531, 2021.

Lundin, R., Barabash, S., Yamauchi, M., Nilsson, H., and Brain, D.: On the relation between plasma escape and the Martian crustal magnetic field: PLASMA ESCAPE AND MARTIAN MAGNETIC FIELD, Geophys. Res. Lett., 38, n/a-n/a, https://doi.org/10.1029/2010GL046019, 2011.

365 Mahaffy, P. R., Benna, M., Elrod, M., Yelle, R. V., Bougher, S. W., Stone, S. W., and Jakosky, B. M.: Structure and composition of the neutral upper atmosphere of Mars from the MAVEN NGIMS investigation: STATE OF THE UPPER ATMOSPHERE OF MARS, Geophys. Res. Lett., 42, 8951–8957, https://doi.org/10.1002/2015GL065329, 2015a.

Mahaffy, P. R., Benna, M., King, T., Harpold, D. N., Arvey, R., Barciniak, M., Bendt, M., Carrigan, D., Errigo, T., Holmes, V., Johnson, C. S., Kellogg, J., Kimvilakani, P., Lefavor, M., Hengemihle, J., Jaeger, F., Lyness, E., Maurer, J., Melak, A.,
370 Noreiga, F., Noriega, M., Patel, K., Prats, B., Raaen, E., Tan, F., Weidner, E., Gundersen, C., Battel, S., Block, B. P., Arnett, K., Miller, R., Cooper, C., Edmonson, C., and Nolan, J. T.: The Neutral Gas and Ion Mass Spectrometer on the Mars Atmosphere and Volatile Evolution Mission, Space Sci Rev, 195, 49–73, https://doi.org/10.1007/s11214-014-0091-1, 2015b.

McFadden, J. P., Kortmann, O., Curtis, D., Dalton, G., Johnson, G., Abiad, R., Sterling, R., Hatch, K., Berg, P., Tiu, C., Gordon, D., Heavner, S., Robinson, M., Marckwordt, M., Lin, R., and Jakosky, B.: MAVEN SupraThermal and Thermal Ion
375 Compostion (STATIC) Instrument, Space Sci Rev, 195, 199–256, https://doi.org/10.1007/s11214-015-0175-6, 2015.

Mitchell, D. L., Mazelle, C., Sauvaud, J.-A., Thocaven, J.-J., Rouzaud, J., Fedorov, A., Rouger, P., Toublanc, D., Taylor, E., Gordon, D., Robinson, M., Heavner, S., Turin, P., Diaz-Aguado, M., Curtis, D. W., Lin, R. P., and Jakosky, B. M.: The MAVEN Solar Wind Electron Analyzer, Space Sci Rev, 200, 495–528, https://doi.org/10.1007/s11214-015-0232-1, 2016.

Morschhauser, A., Lesur, V., and Grott, M.: A spherical harmonic model of the lithospheric magnetic field of Mars, J.
380 Geophys. Res. Planets, 119, 1162–1188, https://doi.org/10.1002/2013JE004555, 2014.

Nielsen, E., Fraenz, M., Zou, H., Wang, J.-S., Gurnett, D. A., Kirchner, D. L., Morgan, D. D., Huff, R., Safaeinili, A., Plaut, J. J., Picardi, G., Winningham, J. D., Frahm, R. A., and Lundin, R.: Local plasma processes and enhanced electron densities in the lower ionosphere in magnetic cusp regions on Mars, Planetary and Space Science, 55, 2164–2172, https://doi.org/10.1016/j.pss.2007.07.003, 2007.

385   Rodger, A. S., Moffett, R. J., and Quegan, S.: The role of ion drift in the formation of ionisation troughs in the mid- and high-latitude ionosphere—a review, Journal of Atmospheric and Terrestrial Physics, 54, 1–30, https://doi.org/10.1016/0021-9169(92)90082-V, 1992.

Schunk, R. and Nagy, A.: Ionospheres: Physics, Plasma Physics, and Chemistry, 2nd ed., Cambridge University Press, Cambridge, https://doi.org/10.1017/CBO9780511635342, 2009.

390   St.-Maurice, J.-P. and Torr, D. G.: Nonthermal rate coefficients in the ionosphere: The reactions of O^+ with N_2, O_2, and NO, J. Geophys. Res., 83, 969, https://doi.org/10.1029/JA083iA03p00969, 1978.

Viggiano, A. A., Morris, R. A., Van Doren, J. M., and Paulson, J. F.: Temperature, kinetic energy, and internal energy dependences of the rate constant and branching fraction for the reaction of O^+ (^4S) with CO_2, The Journal of Chemical Physics, 96, 270–274, https://doi.org/10.1063/1.462514, 1992.

395   Vogt, M. F., Withers, P., Fallows, K., Andersson, L., Girazian, Z., Mahaffy, P. R., Benna, M., Elrod, M. K., Connerney, J. E. P., Espley, J. R., Eparvier, F. G., and Jakosky, B. M.: MAVEN observations of dayside peak electron densities in the ionosphere of Mars, J. Geophys. Res. Space Physics, 122, 891–906, https://doi.org/10.1002/2016JA023473, 2017.

Withers, P.: Ionospheric characteristics above Martian crustal magnetic anomalies, Geophys. Res. Lett., 32, L16204, https://doi.org/10.1029/2005GL023483, 2005.

400   Withers, P., Matta, M., Lester, M., Andrews, D., Edberg, N. J. T., Nilsson, H., Opgenoorth, H., Curry, S., Lillis, R., Dubinin, E., Fränz, M., Han, X., Kofman, W., Lei, L., Morgan, D., Pätzold, M., Peter, K., Opitz, A., Wild, J. A., and Witasse, O.: The morphology of the topside ionosphere of Mars under different solar wind conditions: Results of a multi-instrument observing campaign by Mars Express in 2010, Planetary and Space Science, 120, 24–34, https://doi.org/10.1016/j.pss.2015.10.013, 2016.

405   Withers, P., Flynn, C. L., Vogt, M. F., Mayyasi, M., Mahaffy, P., Benna, M., Elrod, M., McFadden, J. P., Dunn, P., Liu, G., Andersson, L., and England, S.: Mars's Dayside Upper Ionospheric Composition Is Affected by Magnetic Field Conditions, J. Geophys. Res. Space Physics, 2018JA026266, https://doi.org/10.1029/2018JA026266, 2019.

Xu, S., Mitchell, D. L., McFadden, J. P., Fillingim, M. O., Andersson, L., Brain, D. A., Weber, T., Schneider, N. M., Jain, S., Fowler, C. M., Lillis, R., Mazelle, C., and Espley, J.: Inverted-V Electron Acceleration Events Concurring With Localized
410   Auroral Observations at Mars by MAVEN, Geophys. Res. Lett., 47, https://doi.org/10.1029/2020GL087414, 2020.